PHYSICAL REVIEW A **90**, 022510 (2014)

Impact broadening, shifting, and asymmetry of the D_1 and D_2 lines of alkali-metal atoms colliding with noble-gas atoms

L Blank and David E. Weeks[*]
Department of Engineering Physics, Air Force Institute of Technology, 2950 Hobson Way, WPAFB, Ohio 45433-7765, USA

(Received 19 June 2014; published 18 August 2014)

The Anderson Talman theory of spectral line broadening is used together with potential energy curves calculated at the spin-orbit multi-reference configuration interaction level to compute broadening, shifting, and asymmetry coefficients of the D_1 and D_2 lines of alkali-metal atoms M, as they collide with noble gas atoms N, where $M =$ K, Rb, and Cs, and $N =$ He, Ne, and Ar. Our calculated coefficients are compared to experimental results for a variety of temperatures. In all cases general agreement is observed for the broadening coefficients, while significant disagreement is observed for the shifting coefficients. We also compare our K + He broadening and shifting results with fully quantum-mechanical calculations that employ the Baranger theory of collisional line broadening, and we compare our results with other semiclassical calculations. As with the comparison to experiment, closer agreement is observed for the broadening coefficients while the shifting coefficients exhibit significant disagreement. We use the natural variation between the difference potentials of the nine $M + N$ pairs to explore the relationship between potential and line shape as determined by Anderson-Talman theory and develop a picture for the mechanism that underlies the general agreement between theoretical and experimental results on the broadening coefficient and the general disagreement on shifting coefficients.

DOI: 10.1103/PhysRevA.90.022510 PACS number(s): 32.70.Jz

I. INTRODUCTION

Collisionally induced spectral broadening of alkali-metal atoms with noble-gas perturbers has been of significant interest through most of the twentieth century [1]. More recent interest has been generated with the advent of optically pumped alkali-metal-vapor lasers that produce high power with high beam quality [2–6]. These lasers operate by vaporizing a low concentration of alkali-metal atoms into a buffer gas, typically He. The alkali-metal atoms are then pumped from the ground $^2S_{1/2}$ level to the excited $^2P_{3/2}$ level and make a nonadiabatic transition to the $^2P_{1/2}$ level. This establishes a population inversion between the $^2P_{1/2}$ and $^2S_{1/2}$ levels and the system lases on the D_1 line. By controlling the pressure of the buffer gas, the collisionally broadened alkali-metal line shape can be tuned to match a relatively broad optical pump source. Interest in this laser system has prompted measurements of the broadening and shift coefficients of Rb and Cs perturbed by a variety of buffer gases [7,8]. The recent observation of brown dwarfs has also revived interest in the spectral broadening of various alkali-metal atoms [9–13]. The line shape of light alkali metals in the brown-dwarf photosphere provides a useful diagnostic for the atmospheres of these substellar objects [14].

Recently Allard *et al.* [12] used *ab initio* potential energy curves (PECs), calculated with pseudopotential methods for $M +$ He [15] and $M + H_2$ [16], together with a dipole autocorrelation formulation of spectral broadening theory, to determine collisional broadening coefficients for $M =$ Li, Na, and K over a temperature range of 500–3000 K. These calculations employ a classical path approximation and include a dipole transition moment that is functionally dependent on the internuclear separation of the emitter and perturber [17]. The dipole autocorrelation formulation has also been used to compute line profiles of Rb + He and Cs + He [18]. A fully quantum-mechanical calculation by Mullamphy *et al.* [19] employs the Baranger theory of line broadening [20] to calculate broadening and shifting coefficients for temperatures up to 3000 K for Li, Na, and K perturbed by He. Their calculations are based on *ab initio* PECs generated using a three-body approach, where the alkali-metal atom is treated as an ion together with an active electron, and the He atom is represented by a polarizable atomic core.

In this paper we use the semiclassical Anderson-Talman (AT) theory of spectral broadening [1] together with *ab initio* PECs [21] to determine the broadening, shifting, and asymmetry coefficients of $M =$ K, Rb, and Cs perturbed by $N =$ He, Ne, and Ar. The PECs for these calculations are computed at the spin-orbit multiconfiguration interaction singles and doubles level, with two-component effective core potentials used for the alkali-metal atoms. As discussed by Allard *et al.* [12,17], the correction for the variance of the dipole moment with internuclear separation is significant primarily in the wings of the line-shape profile, and for the calculations here we make the approximation that the dipole transition moments are constant and equal to the asymptotic atomic value for the duration of each collision. Broadening, shifting, and asymmetry coefficients are computed for temperatures that range from 50 to 3000 K.

The PECs used for these semiclassical AT calculations are also used in a fully quantum-mechanical calculation [22,23] that employs the Baranger theory of line broadening [20]. This enables a comparison of broadening and shifting coefficients computed using AT theory with coefficients computed using the fully quantum-mechanical Baranger theory without the ambiguity introduced by the use of different PECs. We also compare our AT results with the Baranger results of Mullamphy *et al.* [19] and the dipole autocorrelation results of Allard *et al.* [12] over a broad range of temperatures, and with experiment at a few select temperatures. In general there is better agreement among the various theories and experiment for the broadening coefficient, and at the same time

---

[*] david.weeks@afit.edu

a significant disagreement for the shifting coefficients. This general agreement on broadening coefficient and disagreement on shifting coefficient is investigated by using the natural variation between PECs for all nine $M+N$ pairs to explore the relationship between potential and line shape as determined by AT spectral broadening theory.

II. THEORY

The formulation of the nondegenerate semiclassical AT theory is reviewed by Allard and Kielkopf [1] and extended to handle degenerate atomic levels by Allard *et al.* [17,24]. We briefly summarize the theory here, starting with the nondegenerate case where the line shape is given by $I(\omega,T)$, ω is the angular frequency measured from the unshifted line center, and T is the temperature. The intensity $I(\omega,T)$ is proportional to the Fourier transform of the autocorrelation function $\Phi(s,T)$,

$$I(\omega,T)=\int_{-\infty}^{\infty}\Phi(s,T)e^{i\omega s}ds, \tag{1}$$

where

$$\Phi(s,T)=\exp\{-ng(s,T)\} \tag{2}$$

and

$$g(s,T)=\int_{0}^{\infty}f(v,T)g(s,v)dv \tag{3}$$

with

$$g(s,v)=2\pi\int_{0}^{\infty}b\,db\int_{-\infty}^{\infty}dx_0 \times\left[1-\exp\left\{-i\int_{0}^{s}\hbar^{-1}\Delta V[R(t)]dt\right\}\right]. \tag{4}$$

Here n is the number density of the perturbing gas, s is time, $f(v,T)$ is the Maxwell speed distribution, and $\Delta V(R)$ is the difference potential (DP). The DP is a function of internuclear separation R and is given by $\Delta V(R)=[V_i(R)-V_f(R)]-(E_i-E_f)$ where $V_i(R)$ and $V_f(R)$ are $M+N$ PECs. As $R\to\infty$, $V_i(R)\to E_i$ and $V_f(R)\to E_f$ where E_i and E_f are the initial and final atomic energies of the transition for which the line shape is being calculated.

The full integration used to compute $g(s,v)$ is performed over all space using cylindrical coordinates where the integral over the azimuthal angle yields the factor of 2π in Eq. (4). The emitter is stationary at the origin and the remaining integrations in Eq. (4) are over the impact parameter b and initial condition x_0 of a perturber with reduced mass μ of the $M+N$ pair. The perturber is assumed to move in a straight line with constant speed v in the positive x direction, where $x=x_0+vt$. The straight-line trajectory together with the impact parameter b yields an internuclear separation given by $R(t)=[b^2+(x_0+vt)^2]^{1/2}$. Finally, an average over the Maxwell speed distribution $f(v,T)$ is performed in Eq. (3) to obtain $g(s,T)$ as a function of temperature. As an approximation to the average over speed, the integral in Eq. (3) may be omitted and $g(s,v)$ may instead be evaluated at the average atomic speed $\bar{v}(T)=(8kT/\pi\mu)^{1/2}$, where k is Boltzmann's constant.

In the impact limit the number density of perturbers is low and $g(s,v)$ must be computed for sufficiently large s so that the autocorrelation function given by Eq. (2) decays to zero. In the limit $s\to\infty$, $g(s,v)\to g_I(s,v)$ where $g_I(s,v)$ is a linear function of time,

$$g_I(s,v)=\{\alpha(v)+i\beta(v)\}s+\{\alpha_0(v)+i\beta_0(v)\}. \tag{5}$$

Either an average over speed or the substitution $v=\bar{v}(T)$ yields $g_I(s,T)$ and, through Eqs. (1) and (2), an analytic expression for the intensity,

$$I(\omega,T)=2\exp(-n\alpha_0) \times\left(\frac{n\alpha\cos(-n\beta_0)-(\omega-n\beta)\sin(-n\beta_0)}{(\omega-n\beta)^2+(n\alpha)^2}\right). \tag{6}$$

When $\alpha_0=0$ and $\beta_0=0$ the intensity in Eq. (6) becomes Lorentzian with a half width at half maximum given by $n\alpha$ and a shift given by $n\beta$. In the impact limit, the broadening coefficient α and shifting coefficient β may be written explicitly as

$$\alpha(v)=2\pi v\int_{0}^{\infty}b\,db[1-\cos\{\theta(v,b)\}] \tag{7}$$

and

$$\beta(v)=2\pi v\int_{0}^{\infty}b\,db\sin\{\theta(v,b)\}, \tag{8}$$

where the accumulated phase $\theta(v,b)$ is given by

$$\theta(v,b)=(\hbar v)^{-1}\int_{-\infty}^{\infty}\Delta V[(b^2+x^2)^{1/2}]dx. \tag{9}$$

In Eq. (5), $\alpha_0(v)$ is the intercept of the real part of $g_I(s,v)$ and, as a scale factor for the total line shape in Eq. (6), may be eliminated from consideration by rescaling the intensity. The asymmetry coefficient $\beta_0(v)$ is the intercept of the imaginary part of $g_I(s,v)$ and in Eq. (6) parametrizes the line-shape asymmetry. While expressions for $\alpha(v)$ and $\beta(v)$ in the impact limit are given by Eqs. (7) and (8), there is no corresponding impact-limit expression for $\beta_0(v)$. To compute $\beta_0(v)$, the full integral for $g(s,v)$ in Eq. (4) must be evaluated. For this reason, all calculations of the broadening, shifting, and asymmetry coefficients in this paper are performed using Eq. (4) where a linear fit to $g(s,v)$ is performed in the limit $s\to\infty$. The slope of the linear fit to the real part of $g(s,v)$ is $\alpha(v)$ and the slope and intercept of the linear fit to the imaginary part of $g(s,v)$ are $\beta(v)$ and $\beta_0(v)$, respectively. Even though we use Eq. (4) for all calculations, we are able interpret our results for $\alpha(v)$ and $\beta(v)$ using Eqs. (7) and (8) because we are evaluating $g(s,v)$ in the impact limit of large s.

For each $M+N$ pair there are four PECs, $V_{X\,^2\Sigma_{1/2}}(R)$, $V_{A\,^2\Pi_{1/2}}(R)$, $V_{A\,^2\Pi_{3/2}}(R)$, and $V_{B\,^2\Sigma_{1/2}}(R)$. As the internuclear separation $R\to\infty$, the ground $X\,^2\Sigma_{1/2}$ PEC correlates with the ground $^2S_{1/2}$ alkali-metal level, the excited $A\,^2\Pi_{1/2}$ PEC correlates with the excited $^2P_{1/2}$ alkali-metal level, and the excited $A\,^2\Pi_{3/2}$ and $B\,^2\Sigma_{1/2}$ PECs correlate with the excited $^2P_{3/2}$ alkali-metal level. The four PECs of each $M+N$ pair are used to compute three DPs required by AT theory to calculate the D_1 and D_2 line shapes,

$$\begin{aligned}\Delta V_{\Pi_{1/2}}(R)&=\left(V_{A\,^2\Pi_{1/2}}-V_{X\,^2\Sigma_{1/2}}\right)-E_{D_1},\\ \Delta V_{\Pi_{3/2}}(R)&=\left(V_{A\,^2\Pi_{3/2}}-V_{X\,^2\Sigma_{1/2}}\right)-E_{D_2},\\ \Delta V_{\Sigma_{1/2}}(R)&=\left(V_{B\Sigma_{1/2}}-V_{X\,^2\Sigma_{1/2}}\right)-E_{D_2},\end{aligned} \tag{10}$$

where E_{D_1} and E_{D_2} are the atomic alkali-metal D_1 and D_2 transition energies, subtracted so that $\Delta V \to 0$ as $R \to \infty$.

When nonadiabatic effects are neglected, the D_1 line shape in AT theory is determined by a single DP, $\Delta V_{\Pi_{1/2}}(R)$. The situation is more complicated for the D_2 line shape where two DPs, $\Delta V_{\Pi_{3/2}}(R)$ and $\Delta V_{\Sigma_{1/2}}(R)$, must both be considered when calculating the line shape. This is accomplished by modifying the autocorrelation function in Eq. (2) to include a weighted sum [24] over $g_i(s,T)$, where $i = \Pi_{3/2}, \Sigma_{1/2}$ labels the DP used in Eq. (4) to compute the corresponding $g_i(s,v)$,

$$\Phi(s,T) = \exp\left(-n\sum_i \pi_i g_i(s,T)\right). \tag{11}$$

To determine the weights π_i we make the approximation that the dipole transition moments are constant and equal to the asymptotic atomic value for the duration of each collision. This essentially reduces the dipole autocorrelation formulation of $g_i(s,v)$ discussed by Allard *et al.* [17] to the AT expression in Eq. (4), slightly modified to include a factor of $d_{PS}/(2d_{PS})$. Here the quantity d_{PS} is the dipole matrix element between the ${}^2P_{3/2}$ and ${}^2S_{1/2}$ atomic states. This yields a weight $\pi_i = 1/2$ for each $g_i(s,T)$ used in Eq. (4). As discussed by Allard *et al.* [17], the approximation of constant dipole moment primarily influences the line wing and is not expected to significantly affect the broadening, shifting, and asymmetry coefficients of the line core.

III. DIFFERENCE POTENTIALS

The DPs in Eq. (10) are calculated using $V_{X\,{}^2\Sigma_{1/2}}(R)$, $V_{A\,{}^2\Pi_{1/2}}(R)$, $V_{A\,{}^2\Pi_{3/2}}(R)$, and $V_{B\,{}^2\Sigma_{1/2}}(R)$ PECs [21] and are plotted in Figs. 1–3. Each figure also contains an inset illustrating the asymptotic form of these curves. The variation between these 27 DPs, three for each of the nine $M+N$ pairs, provides a rich computational laboratory to study the relationship between PECs and spectral line shape as determined by AT theory. For all $M+N$ systems, DPs originating from either the $A\,{}^2\Pi_{1/2}$, $A\,{}^2\Pi_{3/2}$, or $B\,{}^2\Sigma^+_{1/2}$ PECs share the same qualitative features.

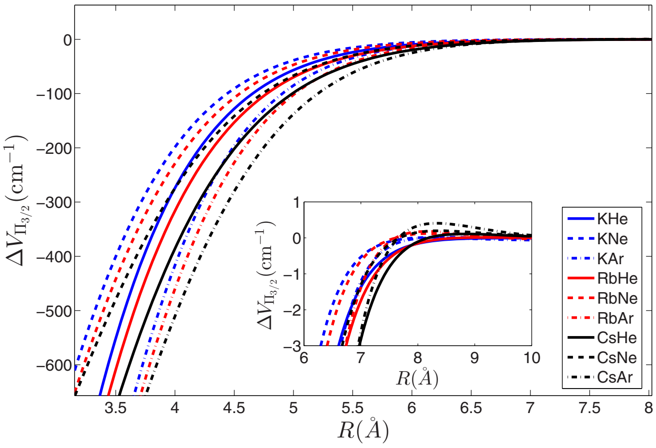

FIG. 2. (Color online) The $\Delta V_{\Pi_{3/2}}$ difference potentials for all $M+N$ combinations.

When considering the approach of a perturber from the asymptotic limit, the $\Delta V_{\Pi_{1/2}}$ DPs plotted in Fig. 1 all slowly rise to a maximum of less than 40 cm^{-1} before decreasing. These maxima are caused in part by a local maximum in the $A\,{}^2\Pi_{1/2}$ PECs together with the wells in the ground $X\,{}^2\Sigma^+_{1/2}$ PECs, both of which occur at roughly the same R. As illustrated in Fig. 2 the $\Delta V_{\Pi_{3/2}}$ DPs essentially decrease as R decreases from the asymptotic limit. This occurs because the onset of the deeper wells in the $A\,{}^2\Pi_{3/2}$ PECs offset the effect of the shallow wells in the $X\,{}^2\Sigma_{1/2}$ ground-state PECs. However, because the onset of the $X\,{}^2\Sigma_{1/2}$ wells occurs at slightly larger R that the onset of the $A\,{}^2\Pi_{3/2}$, there is a very small maximum in the $\Delta V_{\Pi_{3/2}}$ DPs at $R \approx 8$ Å as shown in the inset in Fig, 2. The $\Delta V_{\Sigma_{1/2}}$ DPs are plotted in Fig. 3 and are qualitatively similar to the $\Delta V_{\Pi_{1/2}}$ DPs shown in Fig. 1; however, the maxima of the $\Delta V_{\Sigma_{1/2}}$ DPs occur at much higher energies and for smaller values of R than the maxima exhibited by the $\Delta V_{\Pi_{1/2}}$ DPs. These larger peaks in the $\Delta V_{\Sigma_{1/2}}$ DPs occur because the $V_{B\,{}^2\Sigma_{1/2}}$ PECs all exhibit a barrier as R decreases, followed by a shoulder at fairly high energies. It is the location and shape of these shoulders which

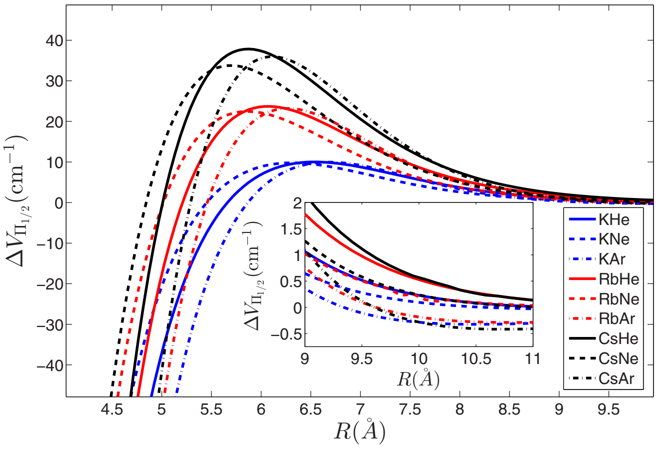

FIG. 1. (Color online) The $\Delta V_{\Pi_{1/2}}$ difference potentials for all $M+N$ combinations.

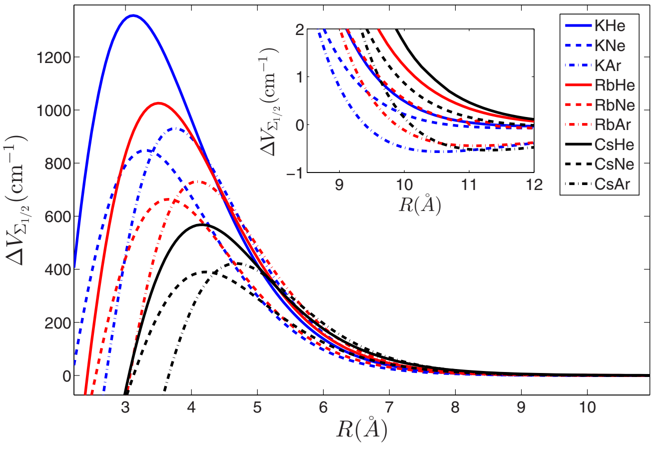

FIG. 3. (Color online) The $\Delta V_{\Sigma_{1/2}}$ difference potentials for all $M+N$ combinations.

give rise to the maxima seen in the $\Delta V_{\Sigma_{1/2}}$ DPs. The energies of these maxima correspond to the frequency, measured from line center, of satellite peaks [21] predicted to appear by the AT theory [1]. At values of $R \approx 10$ Å several of the $\Delta V_{\Sigma_{1/2}}$ DPs exhibit a very shallow well as shown by the inset in Fig. 3. These wells correspond to a very shallow well in the $B\,^2\Sigma^+_{1/2}$ PECs caused by diabatic coupling between the $A\,^2\Pi_{1/2}$ and $B\,^2\Sigma^+_{1/2}$ electronic states.

At values of $R \approx 3.0$ Å all DPs in Figs. 1–3 are decreasing in energy as R decreases. At even smaller values of $R \approx 1$–2 Å not shown in the figures, the DPs turn around and start to increase rapidly in energy with decreasing R.

IV. COMPUTATIONAL DETAILS

The broadening $\alpha(T)$, shifting $\beta(T)$, and asymmetry $\beta_0(T)$ coefficients are calculated by numerically evaluating $g(s,v)$ in Eq. (4). A linear fit to $g(s,v)$ is performed in the impact limit $s \to \infty$ where the slope of the real part of $g(s,v)$ is the broadening coefficient $\alpha(v)$, and the slope and intercept of the imaginary part of $g(s,v)$ are the shifting coefficient $\beta(v)$ and asymmetry coefficient $\beta_0(v)$, respectively. An average over the Maxwell speed distribution is performed to yield the coefficients as a function of temperature.

An analysis of the impact limit of $g(s,v)$ in Eq. (4) used to compute $\alpha(v)$ and $\beta(v)$ can be performed by examining the integrands $\alpha_{\rm int}(v,b)$ and $\beta_{\rm int}(v,b)$ of Eqs. (7) and (8),

$$\alpha_{\rm int}(v,b) = b[1 - \cos\{\theta(v,b)\}] \tag{12}$$

and

$$\beta_{\rm int}(v,b) = b\sin\{\theta(v,b)\}. \tag{13}$$

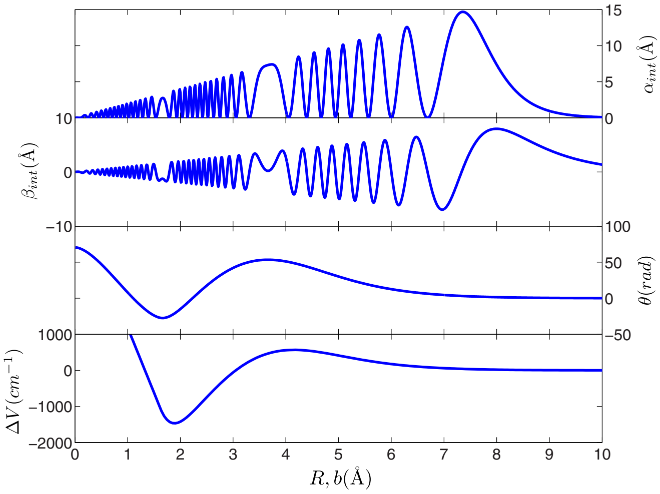

FIG. 4. (Color online) The Cs + He $\Delta V_{\Sigma_{1/2}}$ difference potential is plotted along with the corresponding integrands $\alpha_{\rm int}$ and $\beta_{\rm int}$ given by Eqs. (12) and (13), and $\theta(v,b)$ given by Eq. (9) calculated at $\bar{v}(T = 500$ K). Note that *ab initio* calculations were not performed for $R < 1.6$ Å and the Cs + He $\Delta V_{\Sigma_{1/2}}$ DP is linearly extended for values of $R < 1.6$ Å.

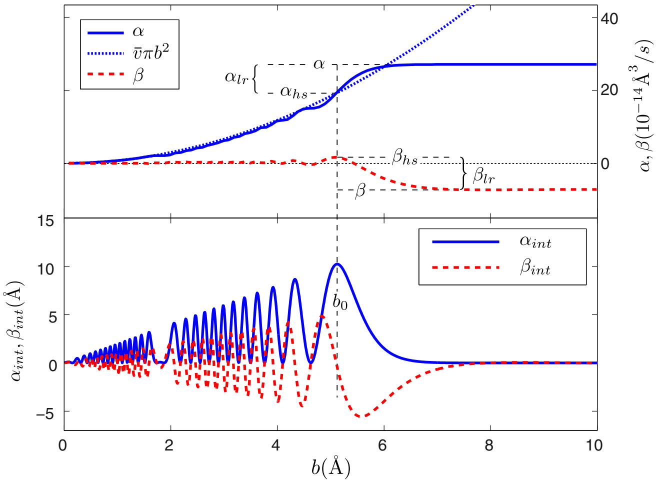

FIG. 5. (Color online) Integrands $\alpha_{\rm int}$ and $\beta_{\rm int}$ given by Eqs. (12) and (13) computed using the Cs + He $\Delta V_{\Pi_{3/2}}$ DP at $\bar{v}(T = 1000$ K) are plotted on the bottom. The integrals $2\pi\bar{v}\int_0^b db'\,\alpha_{\rm int}(b')$ and $2\pi\bar{v}\int_0^b db'\,\beta_{\rm int}(b')$ are plotted on the top and closely follow the effective hard-sphere values until $b = b_0$.

A plot of these integrands calculated using the Cs + He $\Delta V_{\Sigma_{1/2}}$ DP is shown in Fig. 4 along with the $\Delta V_{\Sigma_{1/2}}$ DP and $\theta(v,b)$ as defined in Eq. (9). The total area under the integrands yields α and β up to a factor of $2\pi v$. With the exception of the regions $b \approx 1.8$ Å and $b \approx 3.75$ Å, the integrands rapidly oscillate with some average wavelength $\bar{\lambda}$ until $b = b_0$, where b_0 is defined by the largest value of b for which $\theta(v,b) = \pm\pi$. As b increases beyond b_0, $\alpha_{\rm int}$ decays to zero, and $\beta_{\rm int}$ oscillates for one more quarter cycle and then decays to zero as well. The bounds on the oscillation amplitude for $\alpha_{\rm int}$ are between 0 and $2b$, and and for $\beta_{\rm int}$ are between $-b$ and b. For values of the impact parameter in the range $0 \leqslant b \leqslant b_0$, $\bar{\lambda}$ is large and $\theta(v,b) \sim \bar{\lambda}b$. In the limit of large $\bar{\lambda}$ over this range of b, $\int b\,db\cos(\bar{\lambda}b) \to 0$ and $\int b\,db\sin(\bar{\lambda}b) \to 0$. As a result, when Eqs. (12) and (13) are integrated from $b = 0$ to $b = b_0$ the area under $\alpha_{\rm int}$ is approximately $b_0^2/2$ and the area under $\beta_{\rm int}$ is approximately zero. As illustrated in Fig. 5, the impact parameter $b = b_0$ can therefore be used with Eqs. (7) and (8) to define an effective hard-sphere contribution to the broadening and shifting coefficients,

$$\alpha_{hs}(v,b_0) = 2\pi v\int_0^{b_0} b\,db[1 - \cos\{\theta(v,b)\}]$$

$$\approx v\pi b_0^2 \tag{14}$$

and

$$\beta_{hs}(v,b_0) = 2\pi v\int_0^{b_0} b\,db\sin\{\theta(v,b)\}$$

$$\approx 0. \tag{15}$$

The broadening and shifting coefficients given by Eqs. (7) and (8) may then be reexpressed as the sum of this effective hard-sphere contribution together with a long-range correction,

$$\alpha(v) = \alpha_{hs} + \alpha_{lr}, \tag{16}$$

$$\beta(v) = \beta_{hs} + \beta_{lr},$$

where the long-range corrections are given by

$$\alpha_{lr}(v,b_0) = 2\pi v \int_{b_0}^{\infty} b\, db[1 - \cos\{\theta(v,b)\}] \tag{17}$$

and

$$\beta_{lr}(v,b_0) = 2\pi v \int_{b_0}^{\infty} b\, db \sin\{\theta(v,b)\}. \tag{18}$$

Values of the impact parameter in Eqs. (14) and (15) for which $b < b_0$ correspond to straight-line trajectories that explore the short-range region of the DPs. Any variability in the short-range DPs, and by extension the short-range PECs, will not significantly alter the rapid oscillations of α_{int} and β_{int} for impact parameters $0 \leqslant b \leqslant b_0$. As a result, the effective hard-sphere broadening contribution given by $\alpha_{hs} \approx v\pi b_0^2$ in Eq. (14) is sensitive to the PECs only through the value of b_0, and both broadening and shifting coefficients given by Eqs. (14) and (15) are not sensitive to the details of the short-range PECs for $R < b_0$.

Values of the impact parameter in Eqs. (17) and (18) for which $b > b_0$ correspond to straight-line trajectories that sample the asymptotic region of the DPs. The long-range contributions to the broadening and shifting coefficients given by Eqs. (17) and (18) are therefore sensitive to the DPs, and by extension the PECs, through the value of b_0. Because $\theta(v,b)$ does not rapidly oscillate for $b > b_0$, both $\alpha_{lr}(v,b_0)$ and $\beta_{lr}(v,b_0)$ are also sensitive to the details of the long-range PECs for $R > b_0$. In this long-range region, $\alpha_{\text{int}}(v,b)$ will approach zero as a quadratic function of $\theta(v,b)$ while $\beta_{\text{int}}(v,b)$ will approach zero as a linear function of $\theta(v,b)$. As a result $\alpha_{lr}(v,b_0)$ is less sensitive to the long-range PECs than is $\beta_{lr}(v,b_0)$.

The broadening coefficient $\alpha(v)$ given by Eq. (16) is therefore determined in large part by an effective hard-sphere term α_{hs} that is sensitive to the PECs through the value of b_0, together with a long-range correction term α_{lr} that is sensitive to the long-range details of the PECs through α_{int}, where α_{int} decays quadratically with $\theta(v,b)$ to zero. In contrast, the shifting coefficient $\beta(v)$ given by Eq. (16) is determined almost entirely by the long-range term β_{lr} and is therefore more sensitive to the long-range details of the PECs through β_{int}, where β_{int} decays linearly with $\theta(v,b)$ to zero. This lower sensitivity of $\alpha(v)$ to the details of the PECs yields general agreement between broadening coefficients calculated using different $M + N$ PECs and general agreement with experimental observation. In contrast, the shifting coefficient is more sensitive to the details of the long-range PECs, where a difference of less than a wave number over 10–20 Å can significantly change the value obtained for $\beta(v)$ and may even change the sign of the shifting coefficient. As a result, there can be significant disagreement between various calculations and experimental observations of the shifting coefficient.

This sensitivity of the shifting coefficient to the long-range PECs is also expected to be present in the dipole autocorrelation formulation [17] where the dipole autocorrelation formulation essentially reduces to AT theory in the line core. An increased sensitivity of the shifting coefficient to the long-range PECs compared to the broadening coefficient appears in the full quantum-mechanical Baranger theory [20] as well through the cosine and sine terms in Eqs. (7) and (8) where $\theta(v,b)$ is replaced by $\theta(E,J) = \phi_i(E,J) - \phi_f(E,J)$. In Baranger theory the $\phi_i(E,J)$ and $\phi_f(E,J)$ are scattering phase shifts computed using the $V_i(R)$ and $V_j(R)$ PECs and are functions of kinetic energy E and total angular momentum J [22,23].

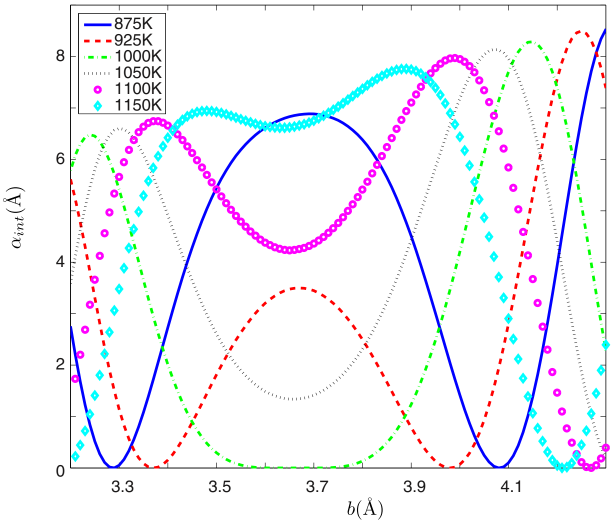

FIG. 6. (Color online) The integrand α_{int} given by Eqs. (12) is computed using the Cs + He $\Delta V_{\Sigma_{1/2}}$ DP for several different values of $\bar{v}$(T) and corresponds to the window of interruption at $b \approx 3.75$ Å in Fig. 4.

It is interesting to note that the rapid oscillation of α_{int} and β_{int} in Fig. 4 is interrupted at impact parameters $b \approx 1.8$ Å and $b \approx 3.75$ Å. These windows of interruption occur at values of b_i where $\theta(v,b_i) = \theta_i$ is an extremum, and the width of the window depends on how rapidly $\theta(v,b)$ varies in the vicinity of the ith extremum. The area under the window of interruption depends on this width and on the value of θ_i. The integrands α_{int} and β_{int} shown in Fig. 4 are calculated using a mean speed $\bar{v}(T) = (8kT/\pi\mu)^{1/2}$ corresponding to a temperature $T = 500$ K. The speed dependence enters the calculation of the integrands through the v^{-1} term in Eq. (9). An increase in $v(T)$ will therefore reduce the overall amplitude of $\theta(v,b)$, causing the θ_i to decrease. As illustrated in Fig. 6, when θ_i changes value, α_{int} and β_{int} will oscillate into and out of these windows of interruption and cause the total area under α_{int} and β_{int} to oscillate. These oscillations are illustrated in Fig. 7 as a function of T for the Cs + He $B\,^2\Sigma^+_{1/2}$ DP where the approximation $v = \bar{v}$ is made. The oscillations are eliminated when the approximation $v = \bar{v}$ is replaced by an average over the Maxwell speed distribution. As illustrated in Fig. 7, the average result can substantially differ from the $v = \bar{v}$ approximation at higher temperatures.

V. RESULTS

The temperature dependence of the broadening coefficients for the D_1 and D_2 alkali-metal line shapes of all $M + N$ combinations is plotted in Figs. 8 and 9, respectively, over a range of $T = 50$–3000 K. These figures show that the broadening coefficient for the $M + N$ pairs is roughly grouped according to noble gas, with M + He combinations showing

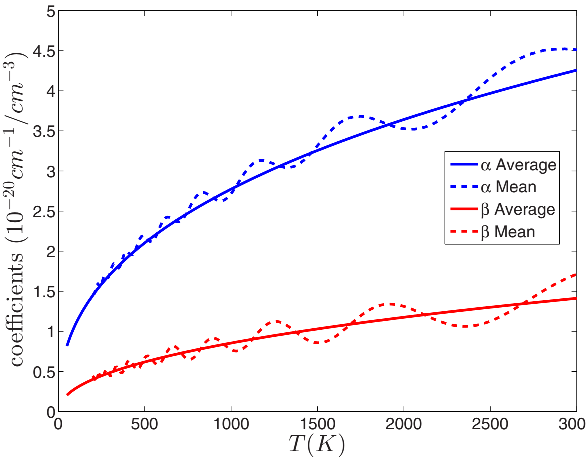

FIG. 7. (Color online) Broadening and shifting coefficients computed using the Cs + He $\Delta V_{\Sigma_{1/2}}$ DP. The α average and β average results are an average over the Maxwell speed distribution while the α mean and β mean results are computed using $\bar{v}(T)$. One cycle of the oscillation of α mean about α average begins with a local maximum at $T = 875$ K, followed by a local minimum at $T = 1000$ K, and ends with a local maximum at $T = 1150$ K, and corresponds to the oscillations of α_{int} into and then back out of the window of interruption in Fig. 6.

the most broadening, followed by M + Ne and then M + Ar. A strong dependence on the noble gas is clearest for the D_2 broadening coefficients, where the argon, neon, and helium groups exhibit no overlap, and is also evident to a lesser degree for the D_1 curves. This trend occurs because the average over speed in Eq. (3) is weighted in favor of $\alpha(v)$ in Eq. (7) for which v is inversely proportional to the square root of the reduced mass.

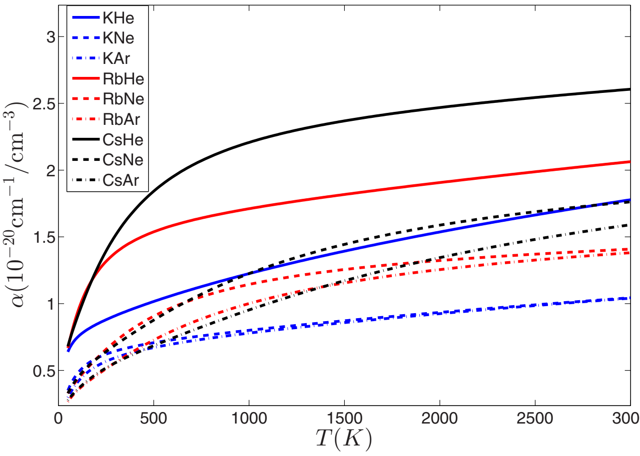

FIG. 8. (Color online) Predicted broadening (half-width) coefficients for the D_1 line of all $M + N$ combinations.

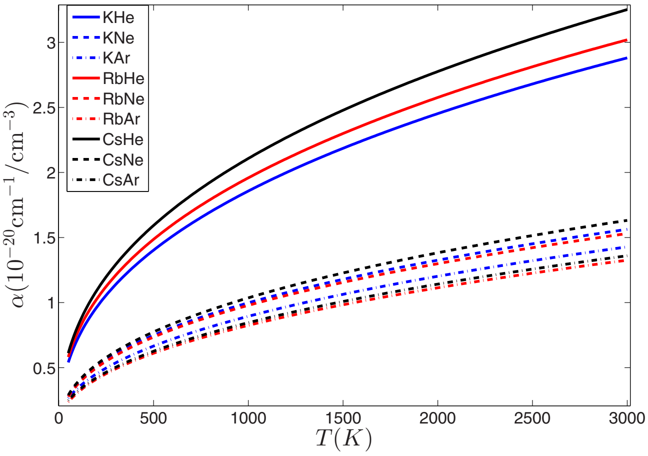

FIG. 9. (Color online) Predicted broadening (half-width) coefficients for the D_2 line of all $M + N$ combinations.

The relationship between DPs and the broadening coefficient $\alpha(T)$ as determined by AT theory is explored in Fig. 10. The value of $R = b_0$ at which the DPs in Fig. 10 exhibit sufficient amplitude for $\theta(v,b_0) = \pm\pi$ defines the effective hard-sphere contribution to $\alpha(T)$. As R decreases from the asymptotic limit in Fig. 10, the $B\,^2\Sigma^+_{1/2}$ DP is the first to depart from zero and reach a value for which $\theta(v,b_0) = \pm\pi$. This is followed at a smaller value of $R = b_0$ for the $A\,^2\Pi_{1/2}$ DP, and then finally the $A\,^2\Pi_{3/2}$ DP. The effective hard sphere contribution to the broadening coefficients, $\alpha_{hs} = v\pi b_0^2$, is therefore largest for $\Delta V_{\Sigma_{1/2}}(R)$ followed by $\Delta V_{\Pi_{1/2}}(R)$, and then $\Delta V_{\Pi_{3/2}}(R)$, and the broadening coefficients $\alpha(T)$ exhibit the same ordering as shown in Fig. 10.

As mentioned in the previous section, an increase in v will reduce the overall amplitude of $\theta(v,b)$ in Eq. (9), and thereby lower the value of $b = b_0$ for which $\theta(v,b_0) = \pm\pi$. The rate at which b_0, and by extension α_{hs}, changes is also a function of the difference potential. As seen in Fig. 11, $b_0 \approx 7.2$ Å at 100 K, and as seen in Fig. 10 the $\Delta V_{\Pi_{1/2}}$ DP is similar to the $\Delta V_{\Sigma_{1/2}}$ DP near $R \approx 7.2$ Å where they are both monotonically decreasing functions of R. As a result, values of α_{hs} computed using $\Delta V_{\Pi_{1/2}}$ will be similar at lower temperatures to values of α_{hs} computed using $\Delta V_{\Sigma_{1/2}}$. At a

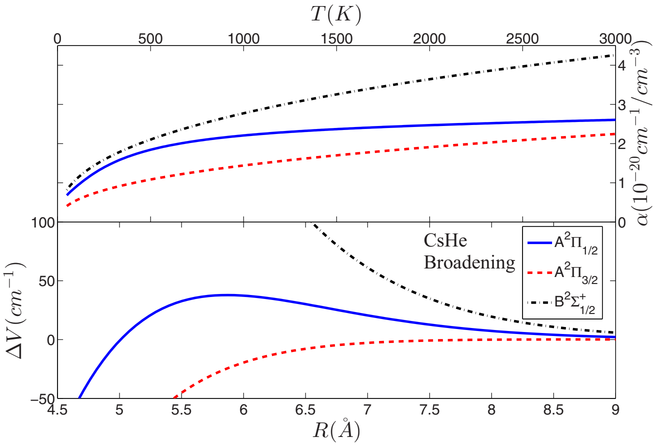

FIG. 10. (Color online) The Cs + He $\Delta V_{\Pi_{1/2}}$, $\Delta V_{\Pi_{3/2}}$, and $\Delta V_{\Sigma_{1/2}}$ DPs are plotted on the bottom and the corresponding broadening coefficients α(T) are plotted on the top. The $A\,^2\Pi_{3/2}$ and $B\,^2\Sigma^+_{1/2}$ broadening coefficients are plotted here separately. Their weighted average in Eq. (11) is used to compute the D_2 broadening coefficient.

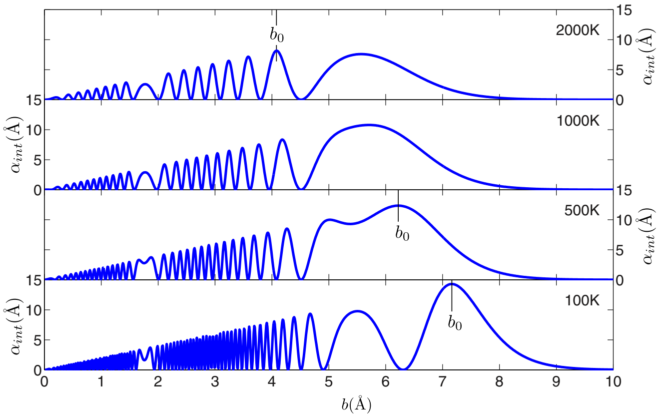

FIG. 11. (Color online) The integrand $\alpha_{\text{int}}(v,b)$ given by Eq. (12) is calculated using the Cs + He $A\,^2\Pi_{1/2}$ DP and plotted for several different temperatures. As the temperature increases from 100 K in the bottom panel to 2000 K in the top panel, the value of b_0 drops from 7.2 Å down to 4.1 Å. As b_0 decreases it crosses through a window of interruption corresponding to the maximum in $\Delta V_{\Pi_{1/2}}$ at $R = 5.9$ Å and becomes somewhat ambiguous at 1000 K.

higher temperature $T = 2000$ K, $b_0 \approx 4.1$ Å in Fig. 11, and as seen in Fig. 10 the $\Delta V_{\Pi_{1/2}}$ DP is similar to the $\Delta V_{\Pi_{3/2}}$ DP near $R \approx 4.1$ Å where they are both monotonically increasing functions of R. As a result, values of α_{hs} computed using $\Delta V_{\Pi_{1/2}}$ will be similar at higher temperatures to values of α_{hs} computed using $\Delta V_{\Pi_{3/2}}$. This behavior is seen in Fig. 10 where the $A\,^2\Pi_{1/2}$ broadening coefficient closely follows the $B\,^2\Sigma_{1/2}$ broadening coefficient at low temperatures and crosses over at higher temperatures to follow the $A\,^2\Pi_{3/2}$ broadening coefficient.

The D_1 and D_2 broadening coefficients plotted in Figs. 8 and 9 are smooth, monotonically increasing functions of temperature and are fit by a power law given by cT^d with fit parameters c and d listed in Table I. The D_2 broadening coefficients are given by the weighted average of the $A\,^2\Pi_{3/2}$ and $B\,^2\Sigma^+_{1/2}$ broadening coefficients in Eq. (11) and are fit to cT^d with residuals that differ from unity by less than 10^{-4} in all cases. This suggests that the $A\,^2\Pi_{3/2}$ and $B\,^2\Sigma^+_{1/2}$ broadening coefficients may be individually fit to cT^d with the same power d. This was verified for all $M + N$ pairs, where the values of d for the $A\,^2\Pi_{3/2}$ and $B\,^2\Sigma^+_{1/2}$ broadening coefficients are essentially identical to the D_2 values of d listed in Table I. The values of the parameter c for the $A\,^2\Pi_{3/2}$ broadening coefficients are smaller than the values of c for the $B\,^2\Sigma^+_{1/2}$ broadening coefficients as seen in Fig. 10 for Cs + He. Note that the residuals listed in Table I for the D_1 fit are smaller than those for the D_2 fit. This is caused by the crossover of the $A\,^2\Pi_{1/2}$ broadening coefficients from $B\,^2\Sigma^+_{1/2}$ behavior at low temperature to $A\,^2\Pi_{3/2}$ behavior at high temperature as shown in Fig. 10 for Cs + He. Note also that the broadening coefficients all have a temperature dependence of $T^{d<1/2}$. If the temperature dependence of the broadening coefficient were solely due to the v term in front of the integral over impact parameter in Eq. (7), then $\alpha(T)$ would be proportional to $T^{d=1/2}$. It is the v^{-1} term in front of the integral for $\theta(b,v)$ in Eq. (9) that gives rise to this reduced value of $d < 1/2$.

TABLE I. Results of fitting the broadening coefficients to a functional from of cT^d where T is in kelvin and the broadening coefficients are in 10^{-20} cm^{-1}/cm^{-3}. These expressions are valid for temperatures ranging from 50 to 3000K.

	D_1			D_2		
$M + N$	c	d	Residual	c	d	Residual
KHe	0.1669	0.2924	0.9873	0.1150	0.4025	1.0000
KNe	0.1802	0.2173	0.9925	0.05803	0.4116	1.0000
KAr	0.1383	0.2507	0.9954	0.04767	0.4246	1.0000
RbHe	0.4631	0.1871	0.9717	0.1262	0.3968	1.0000
RbNe	0.1574	0.2796	0.9594	0.05735	0.4104	1.0000
RbAr	0.07604	0.3674	0.9840	0.04188	0.4316	1.0000
CsHe	0.4114	0.2359	0.9437	0.1329	0.3997	0.9999
CsNe	0.08034	0.3907	0.9902	0.05813	0.4168	1.0000
CsAr	0.03828	0.467	0.9988	0.04299	0.4314	1.0000

The temperature dependence of the shifting coefficients for the D_1 and D_2 line shapes of all $M + N$ combinations is shown in Figs. 12 and 13, respectively. The shifting coefficients are grouped according to noble gas, with the helium curves being the highest, followed by neon, and then finally argon. As with the broadening coefficients, this trend occurs because the average over speed in Eq. (3) is weighted in favor of $\beta(v)$ in Eq. (8) for which v is inversely proportional to the square root of the reduced mass. As illustrated in Fig. 12, the M + He and M + Ne D_1shifting coefficients are all positive over the entire temperature range, while the M + Ar D_1 shifting coefficients are all negative for small T and then all become positive as T increases. It is interesting to note that the K + He D_1 shifting coefficient in Fig. 12 exhibits a maximum at $T \approx 750$ K and then decreases as the temperature increases, and both the K + Ne and K + Ar shifting coefficients increase with temperature until $T \approx 2000$ K where they become constant. In Fig. 13, the M + He and M + Ne D_2 shifting coefficients are also all positive over the entire temperature range while the M + Ar shifting coefficients are all negative over the entire temperature range.

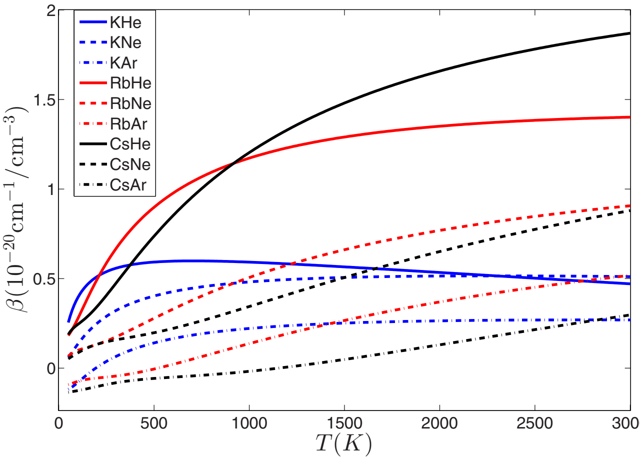

FIG. 12. (Color online) Predicted shifting coefficients for the D_1 line of all $M + N$ combinations.

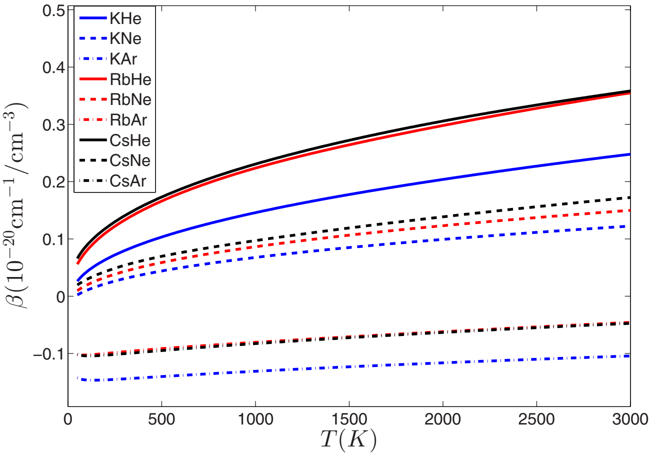

FIG. 13. (Color online) Predicted shifting coefficients for the D_2 line of all $M + N$ combinations.

The relationship between DPs and the shifting coefficient $\beta(T)$ as determined by AT theory is explored in Fig. 14 where it is observed that the $A\,^2\Pi_{1/2}$ and $B\,^2\Sigma^+_{1/2}$ shifts are always positive over the range of T considered while the $A\,^2\Pi_{3/2}$ shifts are always negative. At lower temperatures the sign of the shifting coefficient correlates with the sign of the DP at $R = b_0$, where for $R > 5$ Å, $\Delta V_{\Pi_{1/2}}$ and $\Delta V_{\Sigma 1/2}$ are both positive, while $\Delta V_{\Pi_{3/2}}$ is negative. At higher temperatures, larger values of $\bar{v}(T)$ will lower $\theta(v,b)$ and decrease the value of $b = b_0$. At $b_0 \approx 5$ Å some fraction of the straight-line trajectories in Eq. (9) will begin to explore regions for which $\Delta V_{\Pi_{1/2}}$ is negative. This reduces the rate at which the D_1 shifting coefficient increases and, as seen in Fig. 14, this occurs at a temperature of $T \approx 1000$ K.

As the mass of the alkali-metal atom in the $M + N$ pair decreases, the maximum of the $\Delta V_{\Pi_{1/2}}$ peak in Fig. 1 is observed to decrease. At a fixed temperature and speed, a lower peak height will correspond to a smaller value of b_0 as defined by $\theta(v,b) = \pm\pi$ using Eq. (9). As a result, b_0 will be smallest for K + N followed by b_0 for Rb + N and then Cs + N. For a fixed temperature, the speed will increase as the reduced mass decreases and b_0 will therefor be smallest for K + He, followed by b_0 for K + Ne and then K + Ar. As a result, the straight-line trajectories parametrized by $b \gtrsim b_0$ in Eq. (8) will explore regions for which $\Delta V_{\Pi_{1/2}}$ is negative at lower temperatures for K + N compared to Cs + N and Rb + N. This causes the K + He D_1 shifting coefficient in Fig. 12 to exhibit a maximum at $T \approx 750$ K and then decrease as the temperature increases, and causes both the K + Ne and K + Ar shifting coefficients to increase with temperature until $T \approx 2000$ K, where they become constant. Similar behavior for Rb + N and Cs + N is expected at higher temperatures.

It is interesting to note that the M + Ar $B\,^2\Sigma^+_{1/2}$ DPs shown in the inset of Fig. 3 all exhibit very shallow wells with depths that are on the order of 0.5 cm^{-1}. At temperatures below $T \approx 1500$ K the value of b_0 is sufficiently large so that a majority of trajectories used to compute β_{lr} sample this negative region of the DP. As a result, the $B\,^2\Sigma^+_{1/2}$ shifting coefficients shown in Fig. 15 are negative for $T < 1500$ K, and illustrate the extreme sensitivity of the shifting coefficients to the long-range features of the DPs for $R > b_0$. At higher temperatures $T > 1500$ K, the value of b_0 becomes sufficiently small so that more trajectories used to compute β_{lr} sample the positive region of the DP and $\beta(T)$ becomes positive. Similar behavior is observed for the M + Ar D_1 shifting coefficients in Fig. 12 where the negative shifting coefficients at lower temperatures correspond to the shallow well in the M + Ar $\Delta V_{\Pi_{1/2}}$ DPs shown in the inset in Fig. 1.

The temperature dependence of the asymmetry coefficients for the D_1 and D_2 line shapes of all $M + N$ combinations is shown in Figs. 16 and 17, respectively. As illustrated in Fig. 16, the K + N, Rb + N and Cs + He D_1 asymmetry coefficients at low temperatures either rapidly rise or start at a peak value and then decay back to zero as the temperature

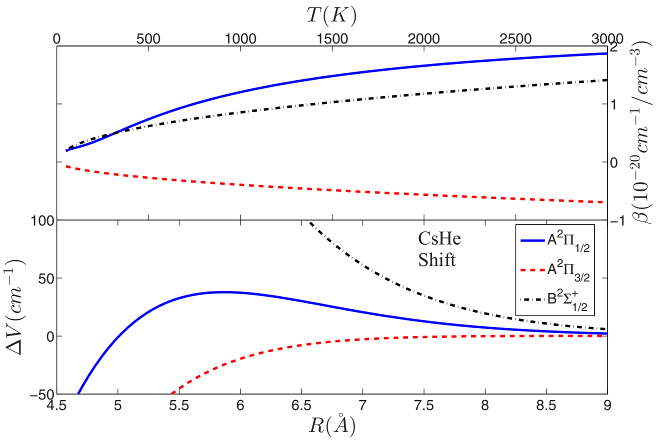

FIG. 14. (Color online) The Cs + He $\Delta V_{\Pi_{1/2}}$, $\Delta V_{\Pi_{3/2}}$, and $\Delta V_{\Sigma_{1/2}}$ DPs are plotted on the bottom and the corresponding shifting coefficients $\beta(T)$ are plotted on the top. The $A\,^2\Pi_{3/2}$ and $B\,^2\Sigma^+_{1/2}$ shifting coefficients are plotted here separately. Their weighted average in Eq. (11) is used to compute the D_2 shifting coefficient.

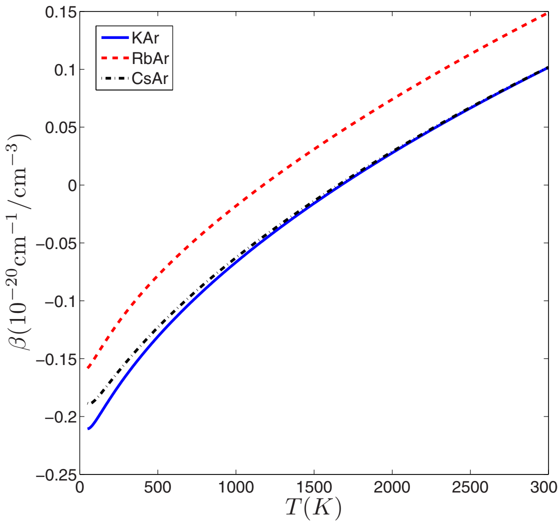

FIG. 15. (Color online) The shifting coefficient $\beta(T)$ computed using the M + Ar $\Delta V_{\Sigma_{1/2}}$ DPs. Negative values of $\beta(T)$ are caused by a very shallow well, approximately 0.5 cm^{-1} deep, in the $\Delta V_{\Sigma_{1/2}}$ DPs shown in the inset in Fig. 3 and illustrate the sensitivity of the shifting coefficients to the PECs.

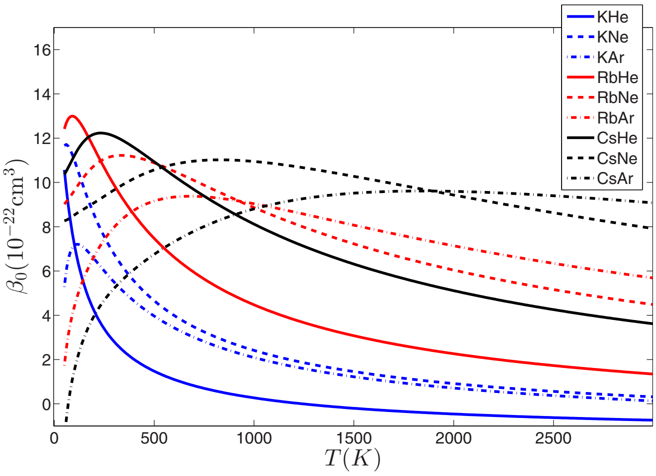

FIG. 16. (Color online) Predicted asymmetry coefficients for the D_1 line of all $M + N$ combinations.

increases, with the K + He D_1 becoming slightly negative. The rate of decay correlates strongly with the alkali-metal atom where the K + N asymmetry coefficients decay most rapidly followed by Rb + N and then Cs + N. For any given alkali-metal atom the asymmetry coefficients decay the most rapidly for helium, followed by neon, and then argon, with the exception of the K + Ar asymmetry coefficient which decays at nearly the same rate as the K + Ne asymmetry coefficient. The D_2 asymmetry coefficients shown in Fig. 17 exhibit the strongest dependence on temperature at lower values of T. As the temperature increases, all of the D_2 asymmetry coefficients become nearly constant with little dependence on temperature at higher values of T.

VI. COMPARISON WITH OTHER WORK

TABLE II. A comparison of broadening and shifting coefficients computed using semiclassical AT theory to experiment and other theory. The Theory B column gives the results of full quantum-mechanical Baranger calculations [22,23] using the same potentials used for the AT results listed in the Theory AT column. Note that radial derivative coupling is ignored for the D_1 coefficients listed in the Theory B column. Temperatures are in kelvin and the coefficients in $10^{-20}\text{cm}^{-1}/\text{cm}^{-3}$. Note that for the K + N combinations the theory was calculated at $T = 410$ K while the experiment gave a range of $T = 400$–420 K.

		Theory AT		Theory B		Expt.		
$M + N$	Temp.	α	β	α	β	α	β	Ref.
KHe								
D_1	410	0.97	0.58	0.91	−0.15	0.82	0.24	[25]
D_2	410	1.29	0.09	1.35	0.01	1.09	0.13	[25]
KNe								
D_1	410	0.68	0.37	0.49	−0.11	0.45	−0.22	[25]
D_2	410	0.69	0.04	0.73	0.06	0.62	−0.33	[25]
KAr								
D_1	410	0.64	0.11	0.52	−0.04	1.30	−1.23	[25]
D_2	410	0.61	−0.14	0.68	−0.18	1.05	−0.81	[25]
RbHe								
D_1	394	1.47	0.79	1.07	−0.82	1.29	0.64	[26]
D_2	394	1.35	0.15	1.45	−0.16	1.36	0.05	[26]
RbNe								
D_1	394	0.82	0.22	0.55	−0.24	0.67	−0.12	[26]
D_2	394	0.67	0.05	0.71	0.00	0.64	−0.33	[26]
RbAr								
D_1	394	0.64	−0.03	0.53	−0.30	1.23	−0.92	[26]
D_2	394	0.55	−0.09	0.67	−0.29	1.20	−0.78	[26]
CsHe								
D_1	323	1.56	0.49	1.13	0.06	1.35	0.47	[7]
D_2	313	1.32	0.14	1.43	0.82	1.11	0.07	[8]
CsNe								
D_1	313	0.70	0.16	0.59	0.03	0.59	−0.17	[7]
D_2	313	0.64	0.05	0.71	0.37	0.53	−0.28	[8]
CsAr								
D_1	313	0.57	−0.08	0.54	0.30	0.99	−0.70	[7]
D_2	313	0.51	−0.10	0.50	0.28	0.89	−0.67	[8]

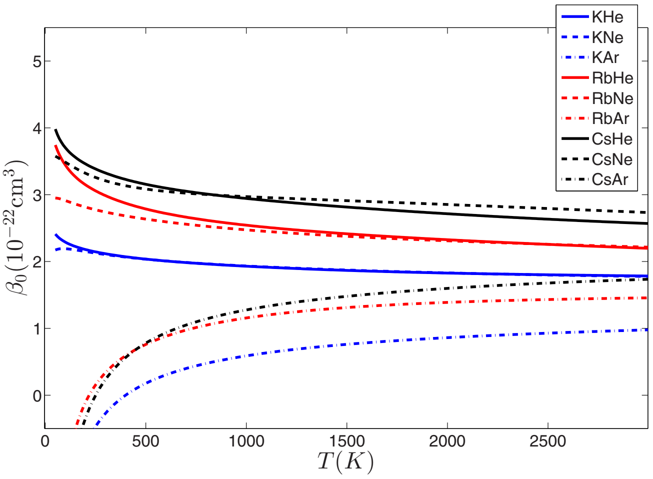

FIG. 17. (Color online) Predicted asymmetry coefficients for the D_2 line of all $M + N$ combinations.

Broadening and shifting coefficients calculated using semiclassical AT theory are compared in Table II with a variety of experimental observations made at specific temperatures. The AT broadening and shifting coefficients are also compared in Table II with broadening and shifting coefficients computed using a fully quantum-mechanical calculation [22,23] that employs the Baranger theory of line broadening [20]. The PECs used for the quantum-mechanical Baranger calculations listed in Table II are the same as those used for the semiclassical AT calculations. This enables the comparison of semiclassical AT results with fully quantum-mechanical Baranger results without the ambiguity introduced by the use of different PECs. The percentage error of the broadening coefficients computed using Baranger theory relative to the broadening coefficients computed using AT theory is in general larger for the D_1 line than for the D_2 line. The largest errors in the D_1 line are ≈30% for K + Ne, Rb + He, Rb + Ne, and Cs + He. The D_2 lines exhibit errors of ≈10% or less with the exception of the Rb + Ar D_2 line with an error of ≈20%. The percentage error of the D_1 and D_2 broadening coefficients computed using AT theory relative to experimental observation are ≈15% with the exception of the M + Ar pairs and the K + Ne D_1 line.

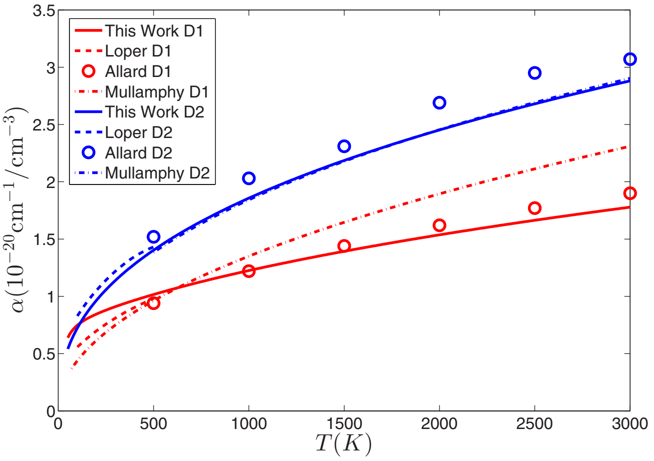

FIG. 18. (Color online) A comparison of broadening coefficients computed using the semiclassical AT theory with other theoretical calculations. Loper [22] and Loper and Weeks [23] compute broadening coefficients using the quantum-mechanical Baranger theory with the same PECs used for the AT calculations. Note that radial derivative coupling is ignored for the Loper D_1 coefficients. Allard *et al.* [12] compute $\alpha(T)$ using the dipole autocorrelation formulation, and Mullamphy *et al.* [19] compute $\alpha(T)$ using quantum-mechanical Barringer theory. Both Allard *et al.* [12] and Mullamphy *et al.* [19] employ different PECs than those used for the AT calculations.

The K + Ne D_1 line exhibits a relative error of ≈30%, and all the M + Ar values are very nearly a factor of 2 too small, most likely because of errors in the long-range region of the M + Ar PECs. There is very little agreement in Table II between shifting coefficients computed using AT theory, shifting coefficients computed using Baranger theory, and experimental shifting coefficients for both the D_1 and D_2 lines.

A comparison of several different theoretical results for the D_1 and D_2 broadening coefficients of K + He is shown in Fig. 18 for a range of temperatures $T = 50$–3000 K. Included in Fig. 18 are broadening coefficients computed using AT theory, broadening coefficients computed using Baranger theory with the same PECs used for the AT calculations [22,23], broadening coefficients computed using Baranger theory with an alternative choice of PECs [19], and broadening coefficients computed using the dipole autocorrelation formulation [12]. Fairly good agreement is observed for the broadening coefficient of the D_2 line given the variety of theoretical models and various PECs used for the calculations. Agreement for the D_1 line remains fairly strong for the broadening coefficients computed using AT theory and the broadening coefficients computed using the dipole autocorrelation formulation [12], with the Mullamphy *et al.* [19] results predicting a somewhat higher value for the D_1 broadening coefficients at higher temperatures.

A similar comparison of several different theoretical results for the D_1 and D_2 shifting coefficients of K + He is shown in Fig. 19 for a range of temperatures $T = 100$–800 K. Included in Fig. 19 are shifting coefficients computed using AT theory, shifting coefficients computed using Baranger theory with the same PECs used for the AT calculations [22,23], and shifting coefficients computed using Baranger theory with an alternative choice of PECs [19]. Unlike the broadening coefficients shown in Fig. 18 there appears to be little agreement between the various calculations, even up to the sign of the shifting coefficient.

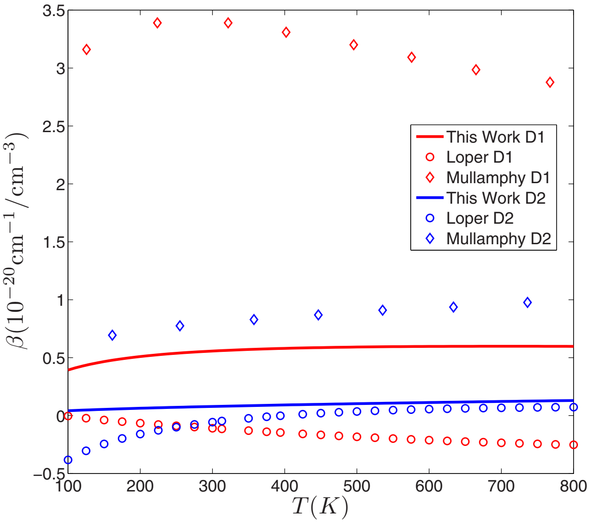

FIG. 19. (Color online) A comparison of Shifting coefficients computed using the semiclassical AT theory with other theoretical calculations. The Loper [22], Loper and Weeks [23], and Mullamphy *et al.* [19] calculations are described in Fig. 18.

The general agreement between broadening coefficients exhibited in Table II and Fig. 18 and general disagreement between shifting coefficients exhibited in Table II and Fig. 19 most likely occurs because the broadening coefficients computed using AT theory are fairly insensitive to the PECs while the shifting coefficients computed using AT theory are very sensitive to the details of the long-range PECs.

Asymmetry coefficients are compared with experiment in Table III. With the exception of the Cs + He D_2 asymmetry coefficient there appears to be significant error in the calculated asymmetries as compared with experiment. In the absence of a simplified expression for β_0 analogous to Eqs. (7) and (8) for the broadening and shifting coefficients, it is difficult to ascertain precisely why this is the case. One possibility is that the intercept of the imaginary part of $g(s,v)$ shares the same sensitivity to the long range PECs as exhibited by the slope of the imaginary part of $g(s,v)$.

VII. CONCLUSIONS

Broadening, shifting, and asymmetry coefficients are computed using the semiclassical AT theory of spectral broadening. The PECs used for these calculations are computed at the spin-orbit multiconfiguration interaction singles and doubles

TABLE III. A comparison of Cs + N asymmetry coefficients computed using semiclassical AT theory with experiment [27] at $T = 323$ T. Coefficients have units of 10^{-20}cm^3.

	CsHe		CsNe		CsAr	
	Theory	Expt.	Theory	Expt.	Theory	Expt.
D_1	12.0	6.2	9.8	6.8	5.4	−41
D_2	3.3	2.7	3.2	− 0.2	0.3	−27

level, with two-component effective core potentials used for the alkali-metal atoms [21]. The broadening, shifting, and asymmetry coefficients computed using AT theory are compared with experimental observations at several different temperatures and are also compared with coefficients computed using the semiclassical dipole autocorrelation formulation of spectral broadening [12], and with two different calculations that use the quantum-mechanical Baranger theory of spectral broadening [19,22,23]. In general there is reasonable agreement on the broadening coefficients and very little agreement on the shifting coefficients between the various theoretical calculations and experiment.

We observe that the broadening coefficients calculated using AT theory may be expressed as the sum of an effective hard-sphere contribution and a long-range contribution. The effective hard-sphere contribution depends on the value of impact parameter for which the accumulated phase has become sufficiently large but is otherwise insensitive to the PECs. The long-range contribution to the broadening coefficient depends on the long-range form of the PECs with an integrand that decays to zero quadratically with the accumulated phase. The shifting coefficients may also be expressed as the sum of an effective hard-sphere contribution and a long-range contribution. However, the effective hard-sphere contribution to the shifting coefficient is approximately zero. As a result, the shifting coefficient is determined almost entirely by the long-range form of the PECs with an integrand that decays linearly to zero with the accumulated phase. This causes the shifting coefficients to be much more sensitive to the details of the long-range PECs compared with the broadening coefficients. We attribute the general agreement on broadening coefficient to the relative insensitivity of $\alpha(T)$ to the PECs, and the general disagreement on the shifting coefficients to the much greater sensitivity of $\beta(T)$ to the PECs. A small difference in the long-range region of the PECs of less than a wave number over 10–20 Å can make a significant difference in the value of the shifting coefficient. This sensitivity of the shifting coefficient to the long-range region of the PECs presents a significant challenge. We also observe that for some systems the difference between coefficients computed using an average over the Maxwell speed distribution and coefficients computed using an average speed can differ on the order of 10%.

Finally, we note that several different PECs may yield nearly the same broadening and shifting coefficients. For example, the shifting and broadening coefficients computed using the DPs in Figs. 1–3 at some particular temperature can be used to compute a set of alternative ΔV_{6-12} DPs [26,28]. While agreement on broadening and shifting coefficients between two different sets of potentials may be achieved at a single temperature, they will in general disagree at different temeperatures. As a result, comparison between various theories and experiment should be made over a range of temperatures whenever possible.

ACKNOWLEDGMENTS

The authors are grateful to G. P. Perram and G. D. Hager for many useful discussions regarding the Anderson-Talman model of spectral line broadening. We gratefully acknowledge support for this work from the Air Force Office of Scientific Research and the High Energy Laser Joint Technology Office. We would also like to acknowledge the Department of Defense High Performance Computer Modernization Program and the AFRL DSRC for computer time and support.

[1] N. Allard and J. Kielkopf, Rev. Mod. Phys. **54**, 1103 (1982).
[2] W. Krupke, R. Beach, V. Kanz, and S. Payne, Opt. Lett. **28**, 2336 (2003).
[3] R. J. Beach, W. F. Krupke, V. K. Kanz, and S. A. Payne, J. Opt. Soc. Am. B **21**, 2151 (2004).
[4] B. V. Zhdanov, T. Ehrenreich, and R. J. Knize, Opt. Commun. **260**, 696 (2006).
[5] R. H. Page, R. J. Beach, V. K. Kanz, and W. F. Krupke, Opt. Lett. **31**, 353 (2006).
[6] B. V. Zhdanov, J. Sell, and R. J. Knize, Electron. Lett. **44**, 582 (2008).
[7] G. A. Pitz, D. E. Wertepny, and G. P. Perram, Phys. Rev. A **80**, 062718 (2009).
[8] G. A. Pitz, C. D. Fox, and G. P. Perram, Phys. Rev. A **82**, 042502 (2010).
[9] S. Seager and D. D. Sasselov, Astrophys. J. **537**, 916 (2000).
[10] A. J. Burgasser, J. D. Kirkpatrick, J. Liebert, and A. Burrows, Astrophys. J. **594**, 510 (2003).
[11] C. Zhu, J. F. Babb, and A. Dalgarno, Phys. Rev. A **73**, 012506 (2006).
[12] N. F. Allard, J. F. Kielkopf, and F. Allard, Eur. Phys. J. D **44**, 507 (2007).
[13] R. Santra and K. Kirby, J. Chem. Phys. **123**, 214309 (2005).
[14] N. F. Allard, A. Nakayama, F. Stienkemeier, J. F. Kielkopf, G. Guillon, and A. Viel, J. Adv. Space Res. (2013), doi:10.1016/j.asr.2013.08.032.
[15] J. Pascale, Phys. Rev. A **28**, 632 (1983).
[16] F. Rossi and J. Pascale, Phys. Rev. A **32**, 2657 (1985).
[17] N. F. Allard, A. Royer, J. F. Kielkopf, and N. Feautrier, Phys. Rev. A **60**, 1021 (1999).
[18] N. F. Allard and F. Speigelman, Astron. Astrophys. **452**, 351 (2006).
[19] D. F. T. Mullamphy, G. Peach, V. Venturi, I. B. Whittingham, and S. J. Gibson, J. Phys. B **40**, 1141 (2007).
[20] M. Baranger, Phys. Rev. **112**, 855 (1958).
[21] L. Blank, G. S. Kedziora, and D. E. Weeks, J. Chem. Phys. **136**, 124315 (2012).
[22] R. D. Loper, Ph.D. thesis, Air Force Institute of Technology, 2013.
[23] R. D. Loper and D. E. Weeks (unpublished).
[24] N. F. Allard, D. Koester, N. Feautrier, and A. Spielfiedel, Astron. Astrophys. Suppl. Ser. **108**, 417 (1994).
[25] N. Lwin and D. G. McCartan, J. Phys. B **11**, 3841 (1978).
[26] M. Rotondaro and G. Perram, J. Quantum Spectrosc. Radiat. Transfer **57**, 497 (1997).
[27] G. D. Hager, G. E. Lott, A. J. Archibald, L. Blank, D. E. Weeks, and G. P. Perram, J. Quantum Spectrosc. Radiat. Transfer (to be published).
[28] W. R. Hindmarsh and J. M. Farr, Prog. Quantum Electron. **2**, 141 (1973).